Distributed inverse synthetic aperture radar imaging of ship target with complex motion

ZHANG Junqiu[1], WANG Yong[1,*], and LU Xiaofei[2]

1. School of Electronics and Information Engineering, Harbin Institute of Technology, Harbin 150001, China;
2. Jiuquan Satellite Launch Center, Jiuquan 732750, China

Abstract: For ship targets with complex motion, it is difficult for the traditional monostatic inverse synthetic aperture radar (ISAR) imaging to improve the cross-range resolution by increasing of accumulation time. In this paper, a distributed ISAR imaging algorithm is proposed to improve the cross-range resolution for the ship target. Multiple stations are used to observe the target in a short time, thereby the effect of incoherence caused by the complex motion of the ship can be reduced. The signal model of ship target with three-dimensional (3-D) rotation is constructed firstly. Then detailed analysis about the improvement of cross-range resolution is presented. Afterward, we propose the methods of parameters estimation to solve the problem of the overlap or gap, which will cause a loss of resolution and is necessary for subsequent processing. Besides, the compressed sensing (CS) method is applied to reconstruct the echoes with gaps. Finally, numerical simulations are presented to verify the effectiveness and the robustness of the proposed algorithm.

Keywords: complex motion, distributed inverse syntheic aperture radar (ISAR), parameters estimation, compressed sensing (CS).

1. Introduction

Inverse synthetic aperture radar (ISAR) imaging is a very important tool for target classification and recognition applications [1]. For advantages of all-weather and all-day capabilities, ISAR technology has received much attention [2]. The ISAR obtains high range resolution by transmitting linear frequency modulated (LFM) signal with wide bandwidth and high cross-range resolution by the synthetic aperture. For targets with smooth motion, such as fast-flying aircraft, cross-range resolution can be improved by extending the coherent processing interval (CPI) in the traditional ISAR system. However, ship tar-

gets tend to move at a low velocity and rotate three-dimensionally with sea waves, which results in complex echoes. There is a contradiction in monostatic ISAR systems that it is difficult to obtain the sufficient accumulation angle when the usable CPI is limited by the complex motion of the target.

To overcome the limitation above, the real antenna array technique was proposed, which obtains the image of target with complex motion in a single snapshot [3,4]. However, the technique with real antenna array greatly increases system complexity and computational burden. Another instantaneous imaging method was proposed to obtain the image of target with complex motion, including the time-frequency analysis method and the LFM signal parameter estimation method. Considering the time-varying characteristic of the Doppler, the range-instantaneous-Doppler (RID) algorithm is applied to image these maneuvering targets [5−10]. However, the instantaneous imaging methods are strongly dependent on the assumed motion model [11,12], which could degrade the image quality when the model is not satisfied.

In this paper, a distributed ISAR algorithm is proposed to image the targets with complex motion in a short CPI. Compared with the monostatic ISAR system, the distributed ISAR system provides multiple virtual equivalent sensors. Hence, the distributed ISAR system has the potential to obtain more spatial sampling data than the monostatic ISAR system at the same time [13]. Moreover, with the guarantee of the same cross-range resolution of the monostatic system, the distributed system requires a shorter CPI. The concept of the distributed ISAR was proposed very early [3], but it has not been further developed due to the limitation of techniques at that time. Some work has promoted further development of the distributed ISAR imaging technology.

The distributed ISAR imaging technology is developed from monostatic ISAR imaging technology. When the single station accumulation angle is insufficient, the radar platforms are separately arranged in the distributed

system to expand the coherent accumulation angle and obtain high cross-range resolution.

In this paper, the distributed ISAR system is divided into two scenarios. The first is the transmit/receive (T/R) distributed ISAR system called multistatic distributed ISAR. In this scenario, only one platform carries a T/R element, and the others only carry the receiving element. The second is the T/R integrated ISAR system called multiple input multiple output (MIMO) distributed ISAR. In this scenario, every platform carries a T/R element, which requires orthogonal waveforms design to distinguish the echoes from different transmitters.

An actual distributed ISAR system is shown in Fig. 1. For simplicity, four stations are presented. Actually, the distance between the ship and the radar is much longer than the baseline length. In the multistatic distributed ISAR, only sensor A transmits LFM signals, and all sensors receive the echoes. In the MIMO distributed ISAR, every sensor transmits and receives echoes, which requires appropriate transmitted waveforms to allow the separation of the echoes.
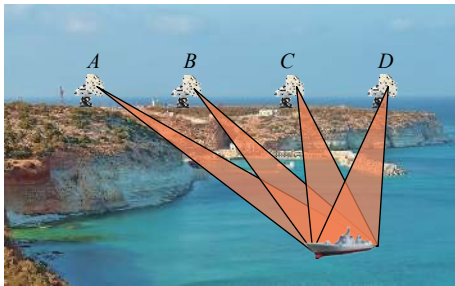

Fig. 1   Distributed ISAR imaging of ship target

The phase center approximation (PCA) [14] theory is suitable in this paper. The PCA theory is described as follows: in certain conditions (such as in the far field), a transmitting element and a receiving element can be approximated by a T/R element, whose position is in the midpoint of the transmitting element and the receiving element [15]. This approximated element is called an equivalent sensor. When the real stations are properly arranged, a wider observation angle will be obtained by the distributed ISAR algorithm.

Depending on the imaging geometry and the rotation of the target, there may be overlaps or gaps between the accumulation angle of two adjacent equivalent sensors [13]. The theoretical derivation of the distributed ISAR algorithm without gap is firstly given to improve cross-range resolution in [16], where smooth motion is assumed, but the method of calculating overlap size is not mentioned.

Based on the derivation of the principle and the numerical simulation, it is concluded that the distributed system can obtain higher cross-range resolution, depending on the number of the stations and their relative positions. However, the number of stations is limited for two reasons: (i) the backscattering coefficient of the target will be different due to the change of the observation angle; (ii) the scattering points occlusion is inevitably in the real targets. These two problems limit the improvement of the cross-range resolution of ISAR imaging [17].

In this paper, the imaging geometry of the ship target with complex motion is presented firstly, with 3-D rotation (roll, pitch, and yaw). Next, the combined imaging method of radar platforms along the cross-range is presented, and the improvement in cross-range resolution is analyzed. Furthermore, the compressed sensing (CS) theory is introduced to solve the observation angle gaps of the adjacent sensors. The numerical simulations are presented to verify the effectiveness and the robustness of the proposed algorithm.

2. Signal model and principle of distributed ISAR imaging algorithm

2.1   Signal model of 3-D rotation ship target

The imaging geometry of the distributed ISAR system is shown in Fig. 2. The ship consists of P scattering points, and their scattering coefficients remain constant approximately in the CPI. With the action of sea waves, the ship target swings in three dimensions.
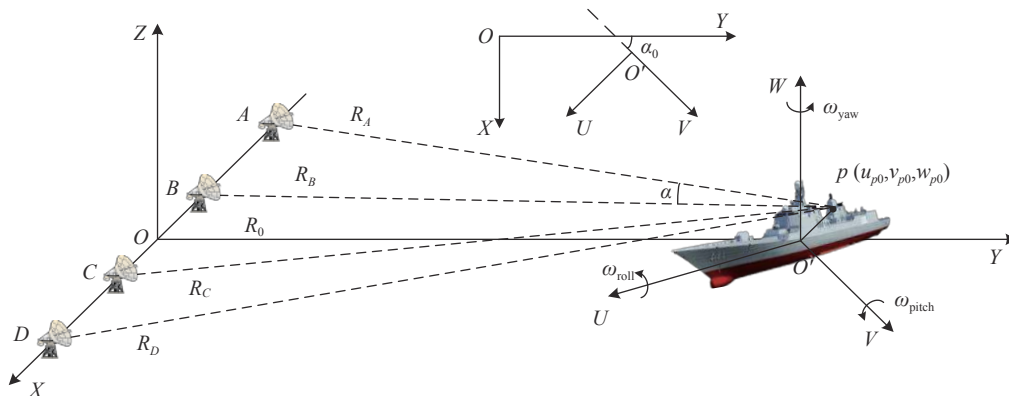

Fig. 2   Imaging geometry of the distributed system

Other than the translation, the target behavior has three degrees of freedom: roll, pitch and yaw. The rotation center of the ship is located at the origin of Cartesian coordinate system (O', U, V, W). Point $p(p = 1, 2, 3, \cdots, P)$ is an arbitrary scattering point of the ship, whose initial coordinate is $(u_{p0}, v_{p0}, w_{p0})^T$.

According to the regular variation law [18] of the target with 3-D rotation, the instantaneous angular variation can be expressed as

$$\theta_l(t) = A_l \cos(\omega_l t + \varphi_l), \ l = \text{roll,pitch,yaw} \quad (1)$$

where A_l is the maximum angular amplitude in radians, ω_l is the rotation velocity, and φ_l is the initial phase of $\theta_l(t)$.

The rotation matrices [19] of roll, pitch and yaw can be expressed as

$$\begin{cases} \mathbf{roll}(\theta_r(t)) = \begin{bmatrix} 1 & 0 & 0 \\ 0 & \cos\theta_r(t) & -\sin\theta_r(t) \\ 0 & \sin\theta_r(t) & \cos\theta_r(t) \end{bmatrix} \\ \mathbf{pitch}(\theta_p(t)) = \begin{bmatrix} \cos\theta_p(t) & 0 & \sin\theta_p(t) \\ 0 & 1 & 0 \\ -\sin\theta_p(t) & 0 & \cos\theta_p(t) \end{bmatrix} \\ \mathbf{yaw}(\theta_y(t)) = \begin{bmatrix} \cos\theta_y(t) & -\sin\theta_y(t) & 0 \\ \sin\theta_y(t) & \cos\theta_y(t) & 0 \\ 0 & 0 & 1 \end{bmatrix} \end{cases} \quad (2)$$

After combining the 3-D rotation matrices in (2), the synthetic rotation matrix $\mathbf{Rot}(t)$ can be expressed as

$$\mathbf{Rot}(t) = \mathbf{roll}(\theta_r(t)) \mathbf{pitch}(\theta_p(t)) \mathbf{yaw}(\theta_y(t)). \quad (3)$$

Then, the position of p in the coordinate system (O', U, V, W) at time t can be described as

$$\begin{bmatrix} u_p(t) \\ v_p(t) \\ w_p(t) \end{bmatrix} = \mathbf{Rot}(t) \begin{bmatrix} u_{p0} \\ v_{p0} \\ w_{p0} \end{bmatrix}. \quad (4)$$

For ship targets, the translational velocity is generally small, and due to the heavy weight of the ship, the translational velocity is generally relatively stable. Therefore, the complex motion of the ship is more reflected in the 3-D rotation with the sea waves. The Doppler of the azimuth signal has a complicated form as

$$f_d(t) = \frac{2f_c}{c} \times \frac{\mathrm{d}}{\mathrm{d}t} \{R(\theta_r(t), \theta_p(t), \theta_y(t))\} \quad (5)$$

where f_c denotes the carrier frequency, c is the light speed, $R(\theta_r(t), \theta_p(t), \theta_y(t))$ is the distance of scattering point and radar.

Assume that the station baseline is perpendicular to the line of sight (LOS) of radar A. Because the distance between the ship and the radar is much longer than the baseline length, the baseline is perpendicular to the LOS of other radars approximately. Radars are located along the X-axis. The angle between the coordinate system

(O, X, Y, Z) and system (O', U, V, W) is α_0. In the coordinate system (O, X, Y, Z), the coordinate of point O' is $(0, R_0, 0)^T$ and the coordinate of p is

$$\begin{bmatrix} x_p(t) \\ y_p(t) \\ z_p(t) \end{bmatrix} = \begin{bmatrix} \cos\alpha_0 & \sin\alpha_0 & 0 \\ -\sin\alpha_0 & \cos\alpha_0 & 0 \\ 0 & 0 & 1 \end{bmatrix} \begin{bmatrix} u_p(t) \\ v_p(t) \\ w_p(t) \end{bmatrix} + \begin{bmatrix} 0 \\ R_0 \\ 0 \end{bmatrix}. \quad (6)$$

It is worth noting that the optimizations of the sensors position in multistatic or MIMO are different. In Fig. 2, a uniform formation is given with baseline length d, and the LOS angular interval between adjacent stations is α approximately. Then, the coordinates of A, B, C, D are

$$\begin{cases} A(-1.5d, 0, 0) \\ B(-0.5d, 0, 0) \\ C(0.5d, 0, 0) \\ D(1.5d, 0, 0) \end{cases}.$$

The distances between sensors and scattering point p at time t can be expressed as

$$\begin{cases} R_p^A(t) = \sqrt{(x_p(t) + 1.5d)^2 + y_p(t)^2 + z_p(t)^2} \\ R_p^B(t) = \sqrt{(x_p(t) + 0.5d)^2 + y_p(t)^2 + z_p(t)^2} \\ R_p^C(t) = \sqrt{(x_p(t) - 0.5d)^2 + y_p(t)^2 + z_p(t)^2} \\ R_p^D(t) = \sqrt{(x_p(t) - 1.5d)^2 + y_p(t)^2 + z_p(t)^2} \end{cases}. \quad (7)$$

The antenna transmits LFM pulse with the form as

$$S_t(\hat{t}, t_m) = \text{rect}\left(\frac{\hat{t}}{T_p}\right) \exp\left[j2\pi\left(f_c t + \frac{1}{2}\gamma\hat{t}^2\right)\right] \quad (8)$$

where $\text{rect}(u) = \begin{cases} 1, & |u| \leqslant 0.5 \\ 0, & |u| > 0.5 \end{cases}$, $\hat{t}$ is the fast time, t_m is the slow time, $t = t_m + \hat{t}$, T_P is the pulse width, and γ represents the frequency modulation rate. The echoes are expressed as

$$S_r^{TR}(\hat{t}, t_m) = \sum_{p=1}^{P} \sigma_p \text{rect}\left(\frac{\hat{t} - R_p^{TR}(t)/c}{T_P}\right) \cdot$$

$$\exp\left[j2\pi\left(f_c\left(t - \frac{R_p^{TR}(t)}{c}\right) + \frac{1}{2}\gamma\left(\hat{t} - \frac{R_p^{TR}(t)}{c}\right)^2\right)\right] \quad (9)$$

where σ_p is the scattering coefficient of scattering p, and $T, R = A, B, C, D$ represent the transmitter and the receiver respectively, and the distances are $R_p^{TR}(t) = R_p^T(t) + R_p^R(t)$.

2.2 Principle of distributed ISAR imaging algorithm

The concept of the abovementioned equivalent sensors is used here. N equivalent sensors can be obtained through S real sensors. Each equivalent sensor independently ob-

serves the target at an angle of $\alpha_n (n = 1, 2, 3, \cdots, N)$. For the short CPI in the distributed system, the target rotates approximately at a constant velocity. Then the accumulated angle can be expressed as $\Delta\theta = \omega T$, where ω is the rotation velocity of the target, T is the CPI.

Assuming the observation time is centered around $t = 0$, the phases of echoes received by sensors $n-1$, n, and $n+1$ in the case with gap are shown in Fig. 3.
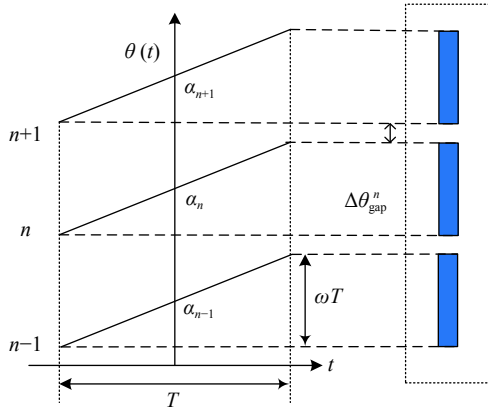

Fig. 3   Phases in the case with gaps between observation angle of adjacent sensors

The observation angle experienced by the equivalent sensor n about time t is given by

$$\theta_n(t) = \alpha_n + \omega t, \ \ n = 1, 2, \cdots, N; -\frac{T}{2} \leqslant t \leqslant \frac{T}{2}. \quad (10)$$

When $\theta_n\left(\dfrac{T}{2}\right) = \theta_{n+1}\left(-\dfrac{T}{2}\right)$, there is no overlap or gap between equivalent sensors n and $n+1$. When $\theta_n\left(\dfrac{T}{2}\right) > \theta_{n+1}\left(-\dfrac{T}{2}\right)$, there will be an overlap between the two adjacent observation angles. When $\theta_n\left(\dfrac{T}{2}\right) < \theta_{n+1}\left(-\dfrac{T}{2}\right)$, there will be a gap which is shown in Fig. 3.

In the case with overlap, the global observation angle of equivalent sensors $n-1$, n, and $n+1$ can be expressed as

$$\Delta\theta_{\text{eff}}^{(n-1,n,n+1)} = \theta_{n+1}\left(\frac{T}{2}\right) - \theta_{n-1}\left(-\frac{T}{2}\right) =$$
$$\left[\alpha_{n+1} + \omega\frac{T}{2}\right] - \left[\alpha_{n-1} - \omega\frac{T}{2}\right] =$$
$$\alpha_{n+1} - \alpha_{n-1} + \omega T. \quad (11)$$

The size of the overlap can be expressed as

$$\Delta\theta_{\text{overlap}}^{n} = \theta_n\left(\frac{T}{2}\right) - \theta_{n+1}\left(-\frac{T}{2}\right) =$$
$$\omega T - (\alpha_{n+1} - \alpha_n). \quad (12)$$

Considering all N equivalent sensors, the global observation angle can be written as

$$\Delta\theta_{\text{eff}} = \theta_N\left(\frac{T}{2}\right) - \theta_1\left(-\frac{T}{2}\right) =$$
$$\alpha_N - \alpha_1 + \omega T. \quad (13)$$

To quantify the improvement of resolution, a parameter γ_{cr} is defined as the ratio between the global observation angle and the single observation angle.

$$\gamma_{cr} = \frac{\Delta\theta_{\text{eff}}}{\Delta\theta} = \frac{\alpha_N - \alpha_1 + \omega T}{\omega T} \quad (14)$$

When there is no overlap or gap between all the equivalent sensors exactly, namely

$$\theta_n\left(\frac{T}{2}\right) = \theta_{n+1}\left(-\frac{T}{2}\right), \ n = 1, 2, 3, \cdots, N-1. \quad (15)$$

The global effective observation angle in (13) can provide the highest cross-range resolution. The relationship of α_n and α_{n+1} is expressed as

$$\alpha_{n+1} - \alpha_n = \omega T, \ n = 1, 2, 3, \cdots, N-1. \quad (16)$$

Then the upper bound of γ_{cr} is

$$\gamma_{cr}^{\max} = \frac{N\omega T}{\omega T} = N. \quad (17)$$

It is worth noting that the overlap part of the observation angle should be estimated and removed before the imaging process.

In the case with gap, the observation angles of the adjacent sensors are separated by a gap size as

$$\Delta\theta_{\text{gap}}^{n} = \theta_{n+1}\left(-\frac{T}{2}\right) - \theta_n\left(\frac{T}{2}\right) =$$
$$(\alpha_{n+1} - \alpha_n) - \omega T. \quad (18)$$

It can be equivalent to the sparse aperture situation of a single station radar. The monostatic ISAR sparse aperture imaging has been studied a lot [13,20,21]. In this paper, the CS method is applied to solve the sparse aperture problem.

The size of the overlap or the gap needs to be obtained for further processing. It can be seen from (12) and (18) that the fundamental issue to calculate the size of overlap or gap is to estimate $\alpha_{n+1} - \alpha_n$ and ω, which is presented in Section 3.

3. Parameters estimation and CS

In this section, the estimation methods of two parameters ω and $\alpha_{n+1} - \alpha_n$ are presented firstly to calculate the size of overlap or gap. Then the CS method is introduced to deal with the sparse aperture problem in the case with gap.

3.1   Target rotation velocity estimation

In this section, the phase frequency modulation method is introduced to estimate the fundamental parameters of the

echoes. Then the slope of the echoes in difference range bins is calculated by linear fitting, and the rotation velocity could be obtained.

Since the antenna configuration has been fixed, only the horizontal rotation can be used for imaging. Point p is located in the plane XOY, and the distance between the point p and the origin O can be expressed approximately as

$$R_p(t) \approx R_0 + x_p \sin(\omega t) + y_p \cos(\omega t). \quad (19)$$

The phase of the echo reflected from the point p can be described as

$$\varphi_p(t) = \frac{4\pi}{\lambda} R_p(t) = \frac{4\pi}{\lambda} [R_0 + x_p \sin(\omega t) + y_p \cos(\omega t)]. \quad (20)$$

Since the CPI in the distributed ISAR system is relatively short, the Taylor expansion of (20) can be expressed as

$$\varphi_p(t) = \frac{4\pi}{\lambda} \left[R_0 + x_p \omega t + y_p - \frac{1}{2} y_p (\omega t)^2 \right]. \quad (21)$$

After translation compensation, the phase of echo in (20) can be expressed as

$$\varphi_p(t) = \frac{4\pi}{\lambda} \left[x_p \omega t + y_p - \frac{1}{2} y_p (\omega t)^2 \right]. \quad (22)$$

The signal in a range bin has an initial frequency $\frac{4\pi x_p \omega}{\lambda}$, and a chirp rate $\frac{4\pi y_p \omega^2}{\lambda}$, which has the form of the LFM signal.

The discrete form of the LFM signal can be expressed as

$$S(m) = \exp\left\{ j \left[\omega_0 m\Delta t + \frac{a(m\Delta t)^2}{2} \right] \right\}, \quad m = 0, 1, \cdots, M-1 \quad (23)$$

where $\Delta t = \frac{1}{f_s}$ is the time sampling interval, f_s is the sampling frequency, m is the discrete time number, ω_0 denotes the initial angular frequency, and a represents the frequency modulation rate. The discrete form of the reference signal is

$$S_{\text{ref}}^0(m) = \exp\left[\frac{ja'(m\Delta t)^2}{2} \right] \quad (24)$$

where a' is the frequency modulation rate to be selected. After multiplying the conjugate reference signal with the original LFM signal, the following expression (25) can be obtained:

$$S_0 = S \cdot S_{\text{ref}}^{0*} = \exp\left\{ j \left[\omega_0 m\Delta t + \frac{a(m\Delta t)^2}{2} - \frac{a'(m\Delta t)^2}{2} \right] \right\}. \quad (25)$$

Suppose $\frac{a(m\Delta t)^2}{2} = \frac{a'(m\Delta t)^2}{2}$ after the careful selection from a range of values of a', then there only exists a single frequency signal. In this paper, the matched filtering method is used to estimate the frequency modulation rate a of the signal. The method of the least squares fitting is applied to optimize the selection of a'. By minimizing the mean square error, the optimization of a' can be obtained. At this point, the fast Fourier transform of (25) is depicted in the following:

$$\text{FFT}(S_0) = \sum_{m=0}^{M-1} \exp\left[j\left(\omega_0 m\Delta t - \frac{2\pi km}{M} \right) \right]. \quad (26)$$

By searching the spectrum peak of the energy distribution of (26), the real initial frequency can be estimated though

$$\omega_0 = \frac{2\pi k}{M\Delta t} \quad (27)$$

where

$$a_0 = a'(i). \quad (28)$$

The rotation velocity is calculated as the following:

$$\omega = \sqrt{\left| \frac{a_0 \lambda}{4\pi} \right|}. \quad (29)$$

Therefore, if the slope of the echoes in difference range bins is obtained, the rotation velocity of the target can be calculated by simple calculation.

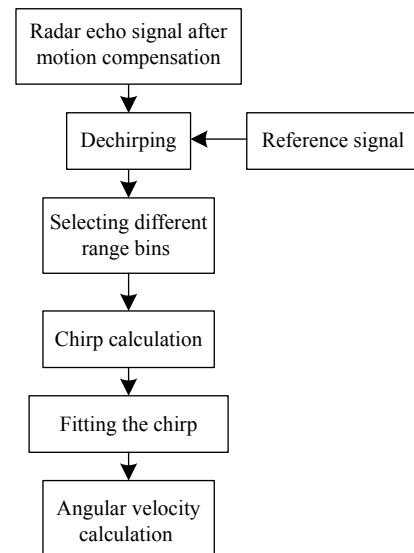The flowchart of the phase frequency modulation method is shown in Fig. 4.

Fig. 4 Flowchart of the phase frequency modulation method

3.2 Station angle estimation

In this section, the observation angle difference $\alpha_{n+1} - \alpha_n$ of the adjacent sensors is addressed as the station

angle. The configuration of the actual antennas determines the positions of the equivalent sensors, which is known in advance. Then the estimation of the station angle is transformed into locating the target. When the target position is known, the station angle could be obtained by simple geometric calculations.

Considering the characteristics of the distributed system, the target can be located by multi-sensor ranging, which avoids the angle measurement with low accuracy. Substitute the distance between the equivalent sensor n and target into

$$S_r^n(\hat{t}, t_m) = \sum_{p=1}^{P} \sigma_p \mathrm{rect}\left(\frac{\hat{t} - 2R_p^n(t_m)/\mathrm{c}}{T_P}\right).$$
$$\exp\left[\mathrm{j}2\pi\left(f_c\left(t - \frac{2R_p^n(t_m)}{\mathrm{c}}\right) + \frac{1}{2}\gamma\left(\hat{t} - \frac{2R_p^n(t_m)}{\mathrm{c}}\right)^2\right)\right]. \quad (30)$$

Both the profile and the phase contain distance information in (30). In a short time, the profile translation of the low-velocity target is not obvious. The estimated profile shift will introduce a larger error. Therefore, the dechirp method is applied to estimate the target distance from the phase term. Ignoring the profile, the reference signal is expressed as

$$S_{\mathrm{ref}}(t) = \exp\left[\mathrm{j}2\pi\left(f_c t + \frac{1}{2}\gamma t^2\right)\right]. \quad (31)$$

After multiplying the conjugate reference signal with the original echoes, the intermediate frequency can be obtained:

$$S_{if}^n(t) = S_r^n(\hat{t}, t_m) \cdot S_{\mathrm{ref}}^* = \sum_{p=1}^{P} \sigma_p.$$
$$\exp\left[-\mathrm{j}2\pi\left(\gamma\frac{2R_p^n(t)}{\mathrm{c}}t + f_c\frac{2R_p^n(t)}{\mathrm{c}} - \gamma\frac{2R_p^n(t)^2}{\mathrm{c}^2}\right)\right]. \quad (32)$$

It can be seen that the signal after dechirp processing is a series of single frequency signals with frequency $\frac{\gamma 2R_p^n(t)}{\mathrm{c}}$, where $p = 1, 2, 3, \cdots, P$. After the Fourier transform of (33), the frequency spectrum related to distances can be obtained. Due to the high range resolution, the target scattering points are located in different range bins after dechirp. It is necessary to set a criterion to determine the center frequency to calculate the target distance. In this paper, taking the amplitude of the 1-D range profile as weights, the center frequency f_w^n is obtained by average. The center frequency f_w^n is used to represent the target location. Then the distance of the equivalent sensor n and the target can be expressed as

$$R_w^n = \frac{\mathrm{c}}{2\gamma}f_w^n. \quad (33)$$

Similarly, the distance between the equivalent sensor

$n+1$ and the target is presented as

$$R_w^{n+1} = \frac{\mathrm{c}}{2\gamma}f_w^{n+1}. \quad (34)$$

According to the law of cosines, the station angle $\alpha_{n+1} - \alpha_n$ can be expressed as

$$\alpha_{n+1} - \alpha_n = \arccos\left(\frac{(R_w^n)^2 + (R_w^{n+1})^2 - (d_n)^2}{2R_w^n R_w^{n+1}}\right) \quad (35)$$

where d_n is the distance of equivalent sensor n and $n-1$.

3.3 CS application in the distributed ISAR

When there is no gap between the observation angles of the adjacent sensors, it needs to estimate the size of the overlap (if any) by (12), then cut off the overlap and combine the echoes directly. When gaps occur, however, a new method is hoped to solve the problem.

In the case with gaps, the azimuth signal is processed by the CS method in this section. The target only occupies a small part in the ISAR image, which means the image is sparse in a certain domain. The information of ISAR data in frequency is redundant. The raw data can be compressed by some techniques, and we can only retain K main components in the sparse domain to recover the data almost perfectly. A common compression technique is the orthogonal transform. Assume a one-dimensional signal $x \in \mathbf{R}^{N \times 1}$ and an orthogonal transformation matrix $\boldsymbol{\Psi}$, where $\boldsymbol{\Psi}\boldsymbol{\Psi}^{\mathrm{H}} = \boldsymbol{\Psi}^{\mathrm{H}}\boldsymbol{\Psi} = \boldsymbol{I}$ ($\boldsymbol{I}$ is the identity matrix). The transformation and the inverse transformation are

$$\begin{cases} y = \boldsymbol{\Psi}x \\ x = \boldsymbol{\Psi}^{\mathrm{H}}y \end{cases} \quad (36)$$

Since the correlation in x is removed, the energy of y is more concentrated. The larger components with the number of K are retained, and the other $N - K$ components are zeroed. After the inverse transformation, the original signal can be reconstructed. We address the signal x with the characteristic above as K sparse signals. The accuracy of signal recovery can be described as relative error in the following:

$$\frac{\|x - \hat{x}\|_2}{\|x\|_2} = \frac{\|y - \hat{y}\|_2}{\|y\|_2} \leqslant \delta \quad (37)$$

where $\hat{x}$ and $\hat{y}$ are the estimated signals, and δ is a small positive number. The abovementioned discussion bases on an assumption that the positions of the K main components have been known, which is illogical in the real system.

The CS method provides another idea for the problem of sparse aperture. Firstly, M times linear measurements of x are made as $s = \boldsymbol{\Phi}x$, $\boldsymbol{\Phi} \in \mathbf{R}^{M \times N}$. Each row of $\boldsymbol{\Phi}$ can be regarded as a sensor, which obtains part information of the signal x. Then it can be described as an optimization problem as

$$\min\|\hat{y}\|_0, \text{ s.t. } \boldsymbol{\Phi}\boldsymbol{\Psi}^{\mathrm{H}}\hat{y} = s. \quad (38)$$

There are two fundamental issues to be considered here: first, how to select the measurement matrix $\boldsymbol{\Phi}$; second, how to deal with the nondeterministic polynomially (NP) problem of the optimization with l_0 norm.

Consider an extreme case where $\boldsymbol{\Phi}$ and $\boldsymbol{\Psi}^{\mathrm{H}}$ are extremely coherent. Specifically, the first M components are considered as the main components. Then the following formula can be obtained:

$$\hat{\boldsymbol{y}} = \begin{array}{c} \boldsymbol{s}^{M \times 1} \\ \boldsymbol{0}^{(N-M) \times 1} \end{array} \qquad (39)$$

which is obviously wrong. It needs to enumerate C_N^K times to get the accurate position of the main component. In contrast, it is more appropriate to make $\boldsymbol{\Phi}$ extremely incoherent with $\boldsymbol{\Psi}^{\mathrm{H}}$. In other words, the measurement matrix $\boldsymbol{\Phi}$ should have the greatest randomness. In this paper, the Gaussian white noise matrix is set as the measurement matrix $\boldsymbol{\Phi}$ and $\boldsymbol{T} = \boldsymbol{\Phi}\boldsymbol{\Psi}^{\mathrm{H}}$ is set as the recovery matrix.

As for the NP problem of the optimization with l_0 norm, it can be converted into l_1 norm in some special cases, which has been proved.

Then the optimization problem can be expressed as

$$\min \|\hat{\boldsymbol{y}}\|_1, \ \text{s.t.} \ \boldsymbol{T}\hat{\boldsymbol{y}} = \boldsymbol{s}. \qquad (40)$$

The azimuth signal in frequency domain is regarded as the signal to be recovered. It only needs to construct a suitable recovery matrix to achieve azimuth imaging.

The CS method set a low bound of echoes number. When there are K important components, the number of observations M is usually four times of K in order to perfectly recover the signal. Mathematically more strictly the number of observations can be limited by $M \geqslant K\log_2\left(\dfrac{N}{K}\right)$, the worse the image quality is.

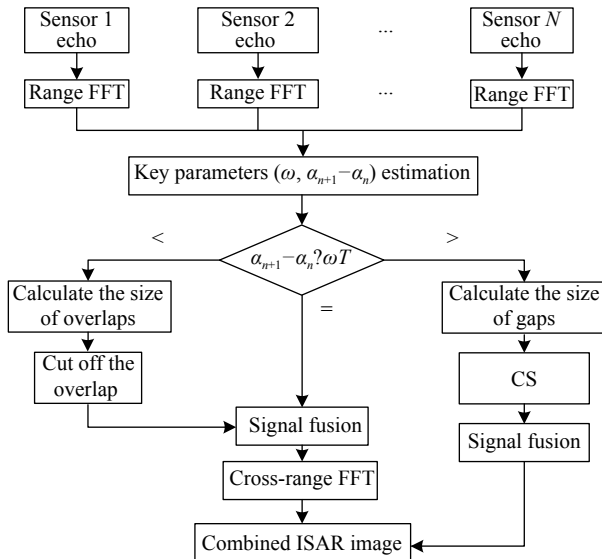Finally, the complete flowchart of the distributed ISAR algorithm is shown in Fig. 5.

Fig. 5   Complete flowchart of the distributed ISAR algorithm

4. Numerical simulations of distributed ISAR

In order to verify the effectiveness and the robustness of the algorithm proposed in this paper, the numerical simulations of ship targets with complex motion are presented in this section.

The parameters of the imaging system are set as Table 1, and the ship model of 66 scattering points is shown in Fig. 6.

Table 1   Simulated system parameters

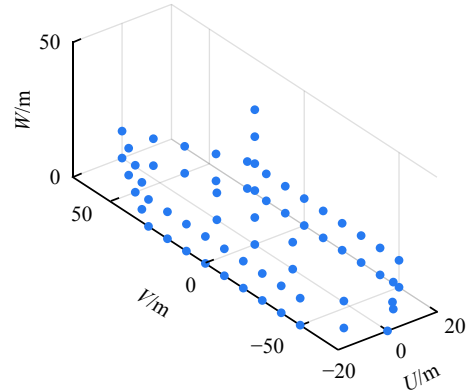| Parameter	Value
Carrier frequency/GHz	3
Bandwidth/MHz	300
Pulse width/μs	1.28
Pulse repetition frequency/kHz	2
CPI/s	0.512

Fig. 6   Ship target scattering points model

The target rotation parameters are shown in Table 2.

Table 2   Simulated target rotation parameters

Parameter	Value
Roll amplitude/(°)	1.00
Pitch amplitude/(°)	0.95
Yaw amplitude/(°)	0.85
Roll angular velocity/(rad·s^{-1})	0.40
Pitch angular velocity/(rad·s^{-1})	0.45
Yaw angular velocity/(rad·s^{-1})	0.48

After the processing of time-frequency analysis, the Doppler of the signal in a certain range bin is presented in Fig. 7. Due to the time-varying Doppler, the cross-range resolution is poor.
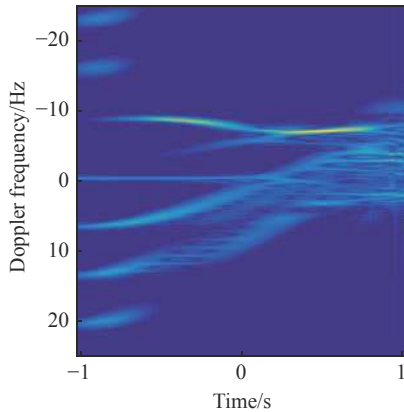
Fig. 7　Doppler frequency of the azimuth signal

The simulations in multistatic and MIMO are respectively given in the following section.

### 4.1　Imaging results of the multistatic distributed ISAR with four stations

The imaging results of the monostatic ISAR is presented in Fig. 8. The image with short CPI before scaling is shown in Fig. 8(a). After the rotation velocity estimation by the phase frequency modulation method, image with real size is shown in Fig. 8(b). For the short CPI, the cross-range resolution is poor, but the ship motion is smooth relatively. When the CPI increases to four times, the image in Fig. 8(c) is obtained, where the resolution of some points is worse than that with short CPI.
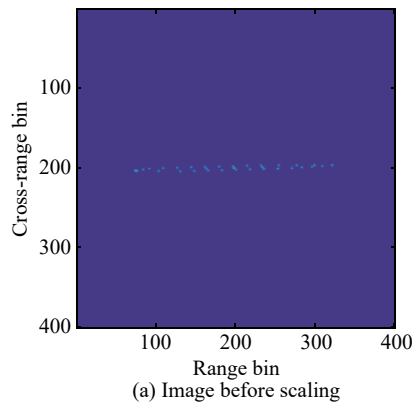
(a) Image before scaling
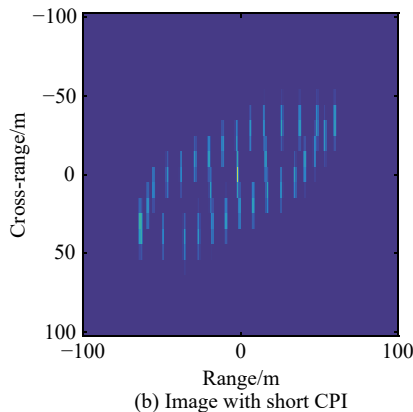
(b) Image with short CPI
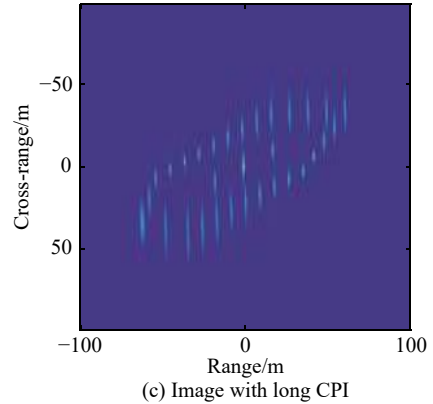
(c) Image with long CPI

Fig. 8　Imaging results of monostatic ISAR system

For the complex motion of the ship, the longer accumulation time does not provide a higher cross-range resolution. Obviously, this traditional ISAR system cannot overcome the contradiction of high resolution and complex motion.

The distributed ISAR can overcome this contradiction very well. In the multistatic ISAR, if the stations are arranged properly, there is no overlap or gap between these four equivalent sensors. One of the optimized multistatic configurations is as follows:

$$\alpha_2 - \alpha_1 = \alpha_3 - \alpha_2 = \alpha_4 - \alpha_3. \tag{41}$$

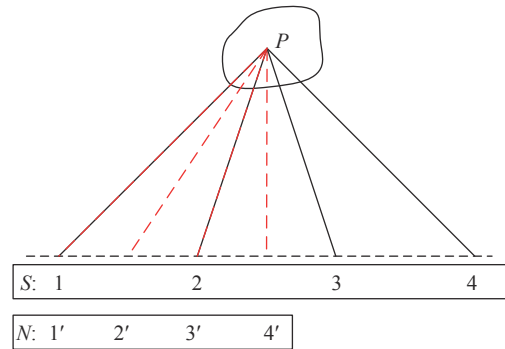The schematic diagram of the optimal arrangement is shown in Fig. 9.

Fig. 9　Schematic diagram of optimized configuration in multistatic

The imaging results of the multistatic distributed ISAR with four stations are shown in Fig. 10. The separate images of four equivalent sensors are shown in Fig. 10(a) to Fig. 10(d) respectively. Their observation time is the same, and the observation angle is slightly different according to the location of the stations. Their images are also slightly different. When there is no overlap or gap between the adjacent sensors, Fig. 10(e) is obtained after multistatic combined imaging. Obviously, the cross-range resolution has been significantly improved. In order to analyze the improvement of resolution, the cross-range point spread function (PSF) in the range bin of −27.5 m is shown in Fig. 10(f). Comparing the width of the main lobe, it can be seen that the proposed algorithm achieves a cross-range resolution improvement of a factor of 4 which is the same as the number of equivalent sensors.
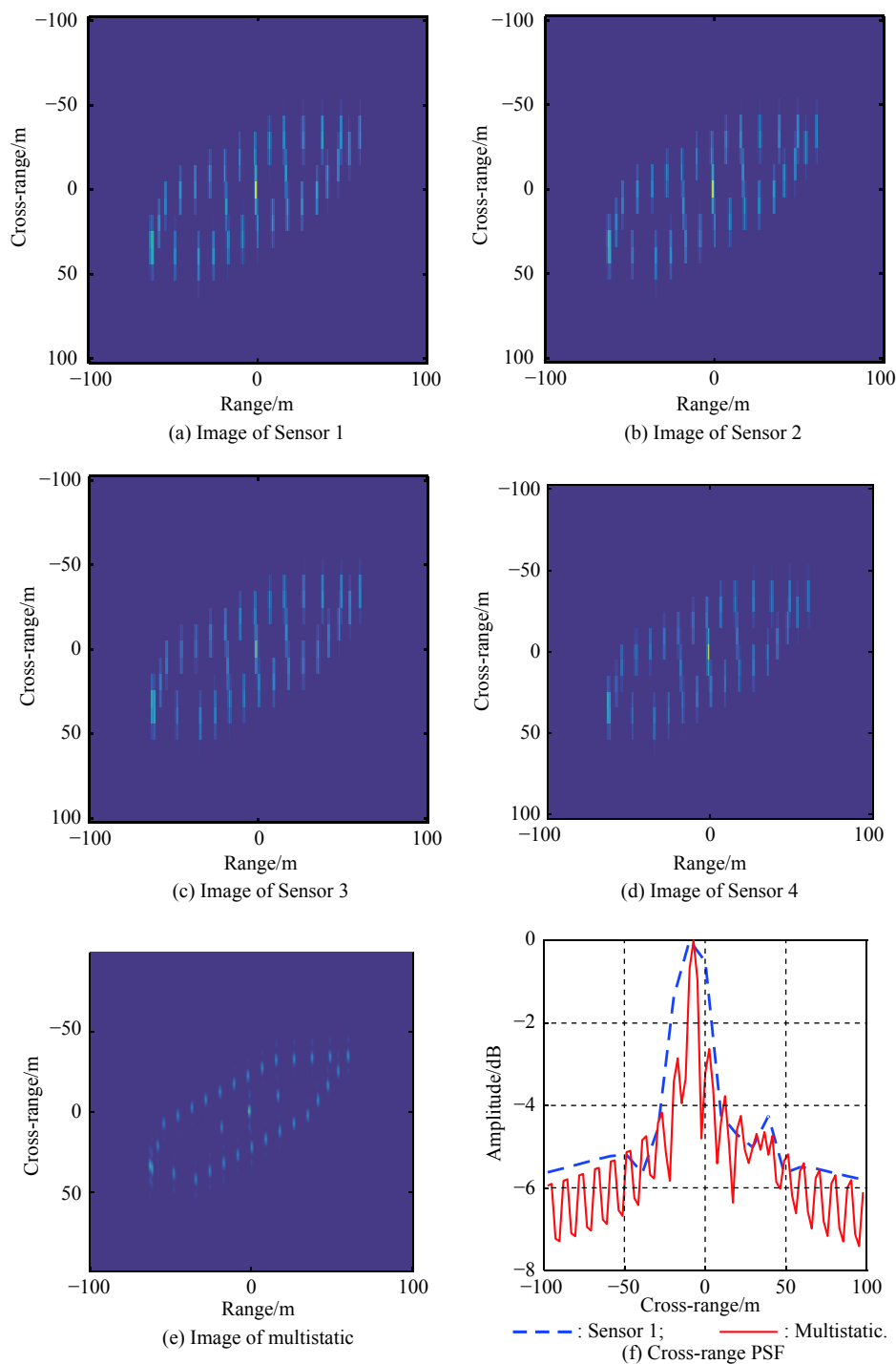
(a) Image of Sensor 1

(b) Image of Sensor 2

(c) Image of Sensor 3

(d) Image of Sensor 4

(e) Image of multistatic

- - - : Sensor 1;   ——— : Multistatic.
(f) Cross-range PSF

Fig. 10   Imaging results of four stations multistatic ISAR system

Images with overlaps or gaps are shown in Fig. 11. Set every overlap or gap part as half of the monostatic entire aperture and get the combined image in Fig. 11(a) and Fig. 11(b) relatively. It can be seen that when there are overlaps or gaps, the cross-range resolution can be improved, but they do not perform well as Fig. 10(e). In the case of overlaps, the actual effective available aperture length is less than that in the case of no overlap or gap, so the improvement is poor. In the case of gaps, the CS method can reconstruct the signal perfectly. However, the sparse aperture in this case is obviously not completely random sparse, which causes the cross-range PSF slightly defocused in Fig. 11(b). The cross-range PSF in the range bin of −27.5 m is shown in Fig. 11(c). It can be seen that

there is the highest cross-range resolution in the case of no overlap or gap. When overlaps or gaps occur, the cross-range resolution will decrease.
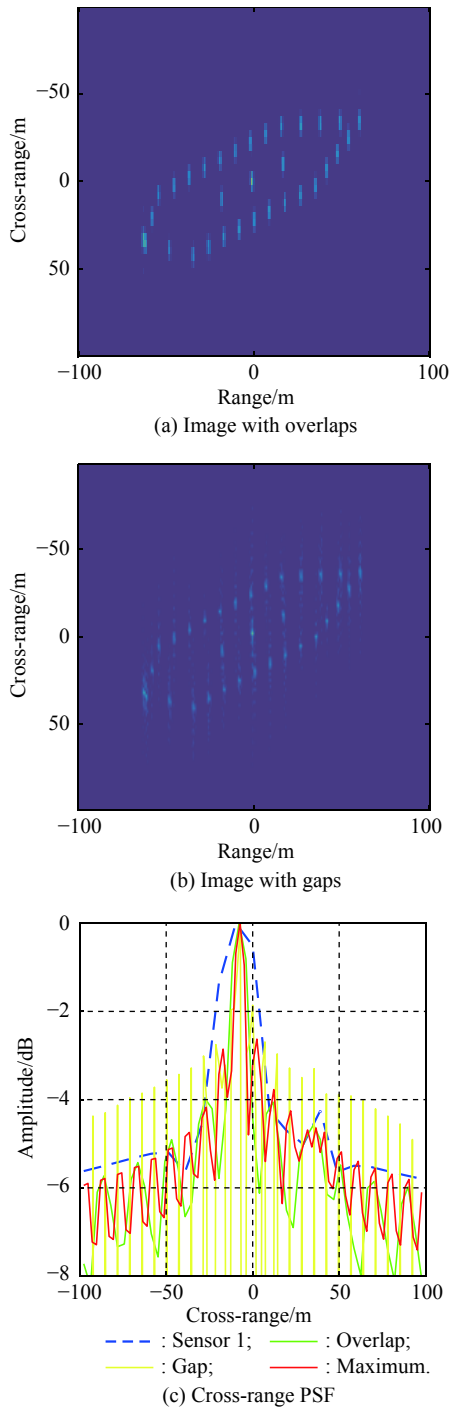

(a) Image with overlaps

(b) Image with gaps

(c) Cross-range PSF

Fig. 11 Imaging results of distributed ISAR system with overlaps or gaps

4.2 Imaging results of the MIMO distributed ISAR with four stations

In the MIMO distributed ISAR, all stations carry trans-

mitting element and receiving element. The number of equivalent sensors can be theoretically expressed as $4 + C_4^2 = 10$. Actually, the resolution cannot be improved up to a factor of 10, because there are overlaps in the observation angles of these equivalent sensors. One of the optimized MIMO configurations is as follows:

$$\begin{cases} \alpha_3 - \alpha_2 = 2(\alpha_2 - \alpha_1) \\ \alpha_4 - \alpha_3 = \alpha_2 - \alpha_1 \end{cases} \tag{42}$$

where α_i is the observation angle of the ith actual sensor.

According to the PCA theory, there are nine equivalent sensors in the MIMO ISAR with four stations. The schematic diagram of optimal arrangement is shown in Fig. 12.
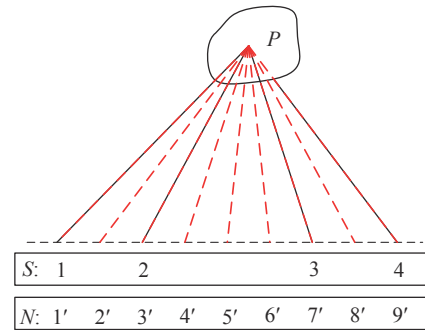

Fig. 12 Schematic diagram of optimized configuration in MIMO

The images of the MIMO distributed ISAR with four stations is shown in Fig. 13. The image of the equivalent sensors 1 is shown in Fig. 13(a). For the short CPI, the cross-range resolution of single sensor image is poor. When there is no overlap or gap between the adjacent sensors, Fig. 13(b) is obtained after MIMO combined imaging. Obviously, the cross-range resolution has been significantly improved. Set every overlap or gap part as half of the monostatic entire aperture and get the combined image in Fig. 13(c) and Fig. 13(d), respectively. It is worth noting that the result of the CS method in Fig. 13(d) is relatively poor. It does not work well as that in the scenario of multistatic. There are more equivalent sensors in the MIMO case, which means more gaps between apertures. For more sparse apertures, the performance of the CS method will be worse. The conclusion can be made that the cross-range resolution cannot be improved indefinitely when there are gaps between the adjacent sensors. The cross-range PSF in the range bin of −27.5 m is shown in Fig. 13(e).

In order to compare the performance of multistatic and MIMO, the cross-range PSFs are shown in Fig. 13(f). It can be seen that with the same number of real stations, MIMO can provide higher resolution.
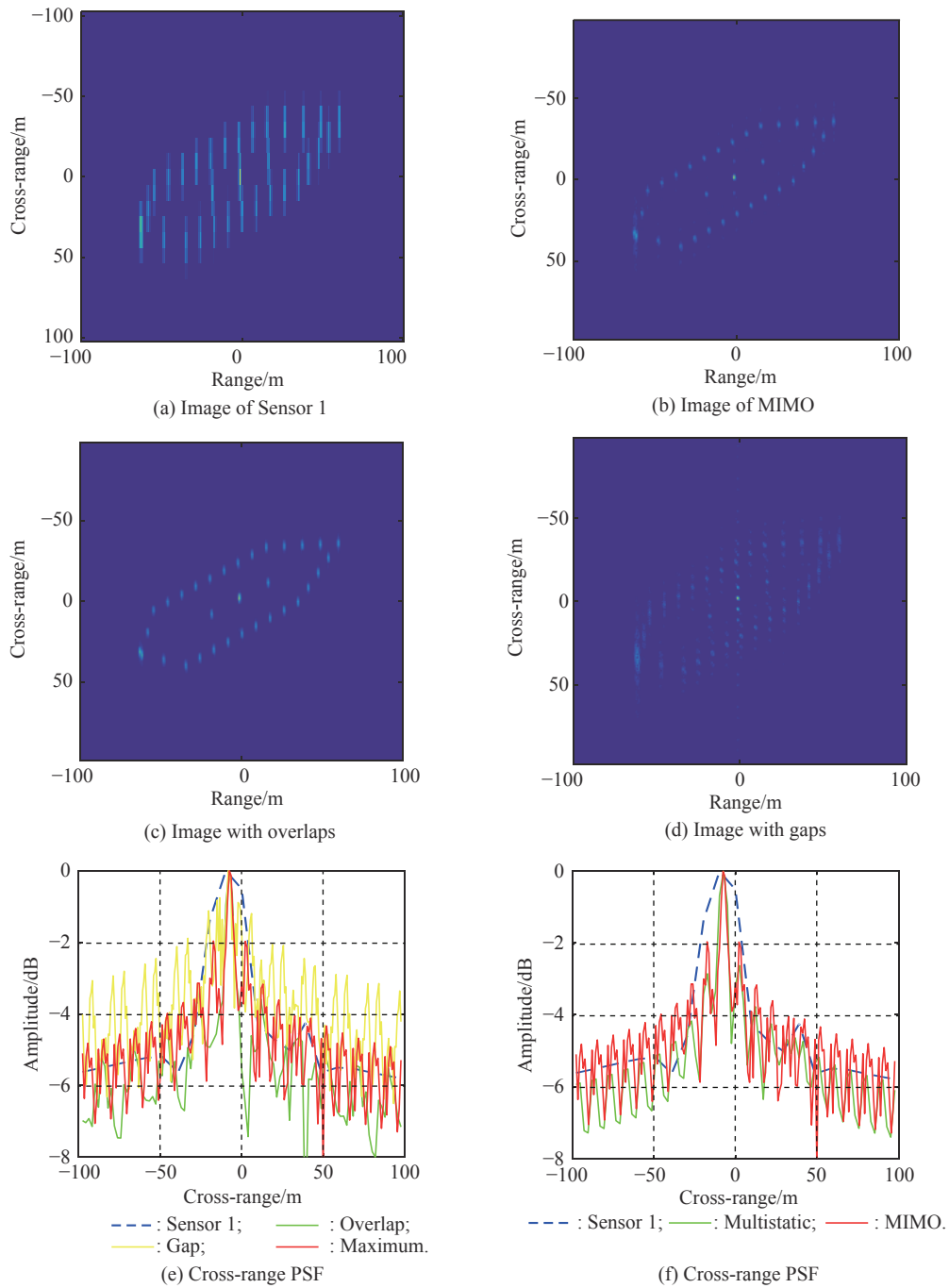
(a) Image of Sensor 1

(b) Image of MIMO

(c) Image with overlaps

(d) Image with gaps

(e) Cross-range PSF
: Sensor 1;   : Overlap;
: Gap;   : Maximum.

(f) Cross-range PSF
: Sensor 1;   : Multistatic;   : MIMO.

Fig. 13   Imaging results of four stations MIMO ISAR system

4.3   Robustness analysis

To verify the robustness of the proposed algorithm, Monte Carlo simulations are presented in various signal-to-noise ratios (SNR). In order to quantify the image quality, the information entropy of the image [22] is introduced. Define the power normalized image as

$$\bar{I}(m,n) = \frac{|I(m,n)|^2}{\sum_m \sum_n |I(m,n)|^2} \tag{43}$$

where $I(m,n)$ is the 2-D image. The 2-D entropy function of radar image is defined as

$$H_e = -\sum_m \sum_n \bar{I}(m,n) \ln\left[\bar{I}(m,n)\right] \tag{44}$$

where the unit is "nat" related to the base of logarithm.

Similar to the 1-D entropy, the 2-D entropy represents the confusion of the image. The higher the entropy, the worse the image quality. When all the power of the image is concentrated in one pixel, its entropy reaches the

minimum value of 0.

In the case of different SNRs, 100 Monte Carlo simulations are carried out. Setting $\omega = 0.01$ rad/s and $\alpha_{n+1} - \alpha_n = 0.005$ rad as the reference value, the estimation values of these experiments are recorded in Table 3.

Table 3   Estimation errors in various SNR

SNR/dB	$\omega'/(\text{rad} \cdot \text{s}^{-1})$	$\Delta\alpha_n'/\text{rad}$
5	0.0155	0.0070
10	0.0139	0.0065
15	0.0125	0.0062
20	0.0114	0.0059
25	0.0110	0.0054
30	0.0108	0.0052
35	0.0102	0.0051

The 2-D image information entropy at different SNRs is shown in Fig. 14. It can be seen that with the increase of SNR, the image entropy gradually decreases, that is, the image quality is improved.
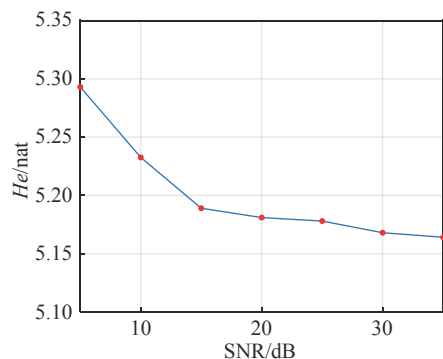

Fig. 14   2-D image entropy at different SNRs

5. Conclusions

To improve the ISAR cross-range resolution of the ship target with complex motion, a novel distributed ISAR algorithm is proposed in this paper. The smooth motion of the target can be approximately considered when the CPI is short enough. However, sufficient cross-range resolution cannot be obtained in the monostatic system with a short CPI. Then the distributed ISAR imaging algorithm is proposed in this paper.

First, the signal model of the ship target with 3-D rotation is constructed. In order to verify the improvement of resolution by distributed ISAR, the increase has been analyzed in details in two scenarios: multistatic and MIMO. There will be a different number of equivalent sensors in these two scenarios. Theoretically, MIMO scenario can provide higher resolution with the same number of real

stations. Nevertheless, the distributed systems lead to some new problems that there will be overlaps or gaps between the observation angles of the adjacent sensors. The phase frequency modulation method is presented to estimate the rotation velocity of the target and the multistatic locating method is presented to estimate the station angle. Finally, the numerical simulations are presented to verify the proposed algorithm.

The contribution in this paper are in the following two aspects. First, the distributed ISAR algorithm is applied to image the ship target with complex motion. The essence of this algorithm is to achieve a transform from the observation of a maneuvering target in a long time to the observation of a stable target in a short time. Second, this paper points out the new problems brought by the distributed system and gives detailed solutions.

Although the proposed algorithm can successfully obtain the high solution images of the targets with complex motion in most applications, it increases the system complexity and computational burden. Compared with the monostatic system, the synchronization errors between stations will also reduce the image quality. In the further research, the analysis of synchronization error and compensation need to be taken seriously to make the proposed algorithm more adaptive and practical.

References

[1] WANG Y X, LING H. A frequency-aspect extrapolation algorithm for ISAR image simulation based on two-dimensional ESPRIT. IEEE Trans. on Geoscience and Remote Sensing, 2000, 38(4): 1743−1748.

[2] XING M D, WU R B, LAN J Q, et al. Migration through resolution cell compensation in ISAR imaging. IEEE Trans. on Geoscience and Remote Sensing, 2004, 1(2): 141−144.

[3] STEINBERG B D. Microwave imaging of aircraft. Proceedings of the IEEE, 1988, 76(12): 1578−1592.

[4] SOUMEKH M. Phase array imaging of moving targets with randomized beam steering and area spotlighting. IEEE Trans. on Image Processing, 1997, 6(5): 736−749.

[5] CHEN V C, QIAN S. Joint time-frequency transform for radar range-Doppler imaging. IEEE Trans. on Aerospace and Electronic Systems, 1998, 34(2): 486−499.

[6] BAO Z, SUN C Y, XING M D. Time-frequency approaches to ISAR imaging of maneuvering targets and their limitations. IEEE Trans. on Aerospace and Electronic Systems, 2001, 37(3): 1091−1099.

[7] XING M, WU R B, LI Y M, et al. New ISAR imaging algorithm based on modified Wigner-Ville distribution. IET Radar, Sonar and Navigation, 2009, 3(1): 70−80.

[8] RUAN H, WU Y H, JIA X, et al. Novel ISAR imaging algorithm for maneuvering targets based on a modified keystone transform. IEEE Geoscience and Remote Sensing Letters, 2014, 11(1): 128−132.

[9] LI L, YAN L, LI D, et al. A novel ISAR imaging method for

maneuvering target based on AM-FM model under low SNR environment. IEEE Access, 2019, 7: 140499−140512.

[10] LI D, GUI X Y, LIU H Q, et al. An ISAR imaging algorithm for maneuvering targets with low SNR based on parameter estimation of multicomponent quadratic FM signals and nonuniform FFT. IEEE Journal of Selected Topics in Applied Earth Observations and Remote Sensing, 2016, 9(12): 5688−5702.

[11] WANG Y, LING H, CHEN V C. ISAR motion compensation via adaptive joint time-frequency technique. IEEE Trans. on Aerospace and Electronic Systems, 2005, 34(2): 670−677.

[12] DU L P, SU G C. Adaptive inverse synthetic aperture radar imaging for nonuniformly moving targets. IEEE Geoscience and Remote Sensing Letters, 2005, 2(3): 247−249.

[13] LI Y Y, FU Y W, ZHANG W P, et al. Distributed ISAR imaging of rotating target based on homotopy L1L0 method. IEEE Sensors Journal, 2020, 20(10): 5452−5464.

[14] BELLETTINI A, PINTO M A. Theoretical accuracy of synthetic aperture sonar micronavigation using a displaced phase center antenna. IEEE Journal of Oceanic Engineering, 2002, 27(4): 780−789.

[15] ZHU Y T, SU Y, YU W X. An ISAR imaging method based on MIMO technique. IEEE Trans. on Geoscience and Remote Sensing, 2010, 48(8): 3290−3299.

[16] PASTINA D, BUCCIARELLI M, LOMBARDO P. Multistatic and MIMO distributed ISAR for enhanced cross-range resolution of rotating targets. IEEE Trans. on Geoscience and Remote Sensing, 2010, 48(8): 3300−3317.

[17] WANG B P, GUO J, CHAO S, et al. An MTRC compensated algorithm based on keystone transform and weighted orientation. Proc. of the International Conference on Consumer Electronics, 2011: 85−89.

[18] YAMANOTO K, IWAMOTO M, KIRIMOTO T. A new algorithm to calculate the reference image of ship targets for ATR using ISAR. Proceedings of the MTS/IEEE Oceans, 2001, 4: 2601–2607.

[19] CHEN V C, MICELI W J. Simulation of ISAR imaging of moving targets. IEE Proceedings on Radar, Sonar Navigation, 2001, 148(3): 160–166.

[20] BAE J H, KANG B S, LEE S H, et al. Bistatic ISAR image reconstruction using spare-recovery interpolation of missing data. IEEE Trans. on Aerospace and Electronic Systems, 2016, 52(3): 1155−1167.

[21] WANG F, EIBERT T F, JIN Y Q. Simulation of ISAR imaging for a space target and reconstruction under space sampling via compressed sensing. IEEE Trans. on Geoscience and Remote Sensing, 2015, 53(6): 3432−3441.

[22] LI X, LIU G S, NI J L. Autofocusing of ISAR images based on entropy minimization. IEEE Trans. on Aerospace and Electronic Systems, 1999, 35(4): 1240−1252.

Biographies

ZHANG Junqiu was born in 1996. He received his B.S. degree in electronic information engineering in 2019 from Harbin Institute of Technology (HIT), Harbin, China. He is now pursuing his Ph.D. degree in the School of Electronics and Information Engineering, HIT. His current research interests include inverse synthetic aperture radar (ISAR) imaging and distributed ISAR.
E-mail: m18134366705@163.com

WANG Yong was born in 1979. He received his B.S. and M.S. degrees in electronic engineering from Harbin Institute of Technology (HIT), Harbin, China, in 2002 and 2004, respectively. He received his Ph.D. degree in information and communication engineering from HIT in 2008. He is currently a professor with the Institute of Electronic Engineering Technology in HIT. His main research interests are time frequency analysis of nonstationary signal, radar signal processing, and their application in SAR imaging.
E-mail: wangyong6012@hit.edu.cn

LU Xiaofei was born in 1981. He received his B.S. and M.S. degrees in electronic engineering from Harbin Institute of Technology (HIT), Harbin, China, in 2002 and 2004, respectively. He received his Ph.D. degree in control theory and control engineering from Tsinghua University in 2012. He is currently an engineer in Jiuquan Satellite Launch Center. His main research interests are target recognition, radar signal processing, and their practical application.
E-mail: luxf08@163.com